JACS
JOURNAL OF THE AMERICAN CHEMICAL SOCIETY
Article
pubs.acs.org/JACS

Cation-Deficient Spinel $ZnMn_2O_4$ Cathode in $Zn(CF_3SO_3)_2$ Electrolyte for Rechargeable Aqueous Zn-Ion Battery

Ning Zhang,[†] Fangyi Cheng,*[,†,‡] Yongchang Liu,[†] Qing Zhao,[†] Kaixiang Lei,[†] Chengcheng Chen,[†] Xiaosong Liu,[§] and Jun Chen[†,‡]

[†]Key Laboratory of Advanced Energy Materials Chemistry (Ministry of Education) and State Key Laboratory of Elemento-Organic Chemistry, College of Chemistry, Nankai University, Tianjin 300071, China

[‡]Collaborative Innovation Center of Chemical Science and Engineering, Nankai University, Tianjin 300071, China

[§]State Key Laboratory of Functional Materials for Informatics, Shanghai Institute of Microsystem and Information Technology, Chinese Academy of Sciences, Shanghai 200050, China

Supporting Information

ABSTRACT: Rechargeable aqueous Zn-ion batteries are attractive cheap, safe and green energy storage technologies but are bottlenecked by limitation in high-capacity cathode and compatible electrolyte to achieve satisfactory cyclability. Here we report the application of nonstoichiometric $ZnMn_2O_4$/carbon composite as a new Zn-insertion cathode material in aqueous $Zn(CF_3SO_3)_2$ electrolyte. In 3 M $Zn(CF_3SO_3)_2$ solution that enables ~100% Zn plating/stripping efficiency with long-term stability and suppresses Mn dissolution, the spinel/carbon hybrid exhibits a reversible capacity of 150 mAh g^{-1} and a capacity retention of 94% over 500 cycles at a high rate of 500 mA g^{-1}. The remarkable electrode performance results from the facile charge transfer and Zn insertion in the structurally robust spinel featuring small particle size and abundant cation vacancies, as evidenced by combined electrochemical measurements, XRD, Raman, synchrotron X-ray absorption spectroscopy, FTIR, and NMR analysis. The results would enlighten and promote the use of cation-defective spinel compounds and trifluoromethanesulfonic electrolyte to develop high-performance rechargeable zinc batteries.

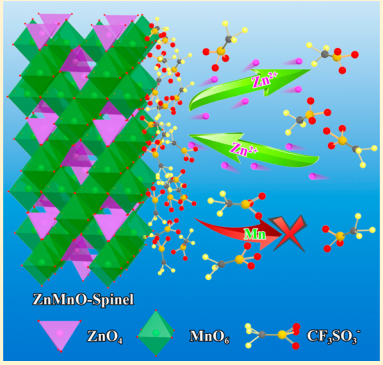

INTRODUCTION

While lithium-ion batteries (LIBs) have gained huge success to power portable electronics and been considered for applications in electric vehicles and large-scale energy storage, there are growing concerns over their cost, safety, environmental impact, and resource limitation.[1,2] In search of alternative battery chemistry, systems based on other lightweight electropositive elements (e.g., Na, Mg, Al, and Ca) have attracted extensive interest because of material abundance and cost effectiveness.[3−8] Meanwhile, the use of aqueous electrolyte to replace organic electrolyte offers advantages including better safety, greener and less rigorous manufacturing conditions, and higher ionic conductivity.[9,10] In this regard, aqueous Zn-ion battery (ZIB) technologies hold particular promise as Zn features low flammability and high water compatibility, and allows multivalent charge transport carriers.[11−16]

Early development of rechargeable alkaline Zn/MnO_2 cells has been plagued by problems such as poor Coulombic efficiency and severe capacity fade due to the formation of unwanted irreversible byproducts, associated with both the manganese oxide cathode (e.g., $Mn(OH)_2$ and Mn_2O_3) and the zinc anode (e.g., $Zn(OH)_2$ or ZnO).[12,13] To improve the electrochemical performance of rechargeable aqueous ZIB, recent efforts take advantage of Zn-ion intercalation/extraction concept and naturally, MnO_2 has been attempted as a Zn-insertion cathode material. For example, tunnel-structured α-MnO_2 and γ-MnO_2 deliver considerable specific capacity up to >200 mAh g^{-1} at low current rates but suffers from limited reversibility that sustains only a few dozens of repeated cycles.[11,14,15] Elaborative electrochemical mechanism investigation reveals that MnO_2 undergoes complex structural transformation from tunnel-type to spinel-type and layered phases on discharging.[14] This transition of structure and phase, along with Mn dissolution via disproportion, leads to poor cyclability of binary manganese oxides. Very recently, the stability of Zn/α-MnO_2 battery was highly improved by using mild aqueous $ZnSO_4$ electrolyte that realizes a proposed conversion reaction between MnOOH and MnO_2.[16] Other cathode materials such as Prussian blue analogues exhibit respectable cycling performance but low capacity (typically ~50 mAh/g).[17−19] Therefore, the development of rechargeable aqueous ZIBs is still in the incipient stage. It is highly desirable to exploit new stable and high-capacity Zn-insertion cathode materials.

Recalling the R&D history of Li-insertion cathodes, a shift from binary metal oxides to lithium metal oxides radically improves the rechargeability, as exemplified by $LiMn_2O_4$ versus

Received: June 10, 2016
Published: September 14, 2016

© 2016 American Chemical Society

DOI: 10.1021/jacs.6b05958
J. Am. Chem. Soc. 2016, 138, 12894−12901

MnO_2.[1,20,21] $LiMn_2O_4$ was also demonstrated to reversibly intercalate Li^+ in aqueous media.[22−24] Considering the analogous spinel structure to $LiMn_2O_4$ and the close ionic radius between Zn^{2+} and Li^+ (0.06 vs 0.059 nm), $ZnMn_2O_4$ (abbreviated as ZMO) is a plausible candidate cathode material for aqueous ZIB. Nevertheless, recent study on chemical extraction of Zn from $ZnMn_2O_4$-based spinel indicates that the ideal spinel structure is unfit for Zn insertion due to the high electrostatic repulsion among Zn^{2+} cations within the lattice.[25] Inspired from the knowledge that the introduction of cation vacancies in other spinel oxides (e.g., $Co_{0.37}Mn_{2.15}O_4$) opens up additional pathways for easier migration of divalent ions (e.g., Mg^{2+}),[26−28] cation-defective $ZnMn_2O_4$ spinel would be a viable Zn insertion host material.

In addition to cathode materials, the search of comparable electrolytes also plays a pivotal importance in developing ZIBs. The KOH-based alkali electrolyte employed in alkaline Zn-MnO_2 battery is not a Zn^{2+} carrier and is detrimental to reversible reaction of zinc anode.[12] Mild acidic electrolyte such as $ZnSO_4$ solution investigated for ZIBs[14,15] suffers from intrinsically limited solubility and Zn stripping/plating Coulombic efficiency. Besides, the effect of zinc salt on the electrochemical performance of aqueous ZIBs remains unclear. Recent studies investigated the electrochemical and transport properties of bulky-anion zinc salts such as zinc bis-(trifluoromethylsulfonyl)imide ($Zn(TFSI)_2$), zinc trifluoromethanesulfonate ($Zn(CF_3SO_3)_2$), zinc tetrafluoroborate ($Zn(BF_4)_2$) and zinc hexafluorophosphate ($Zn(PF_6)_2$) in nonaqueous solvents.[29] Due to the high ionic conductivity and electrochemical stability, $Zn(TFSI)_2$ and $Zn(CF_3SO_3)_2$ have been applied in the organic gel polymer electrolyte for solid-state Zn batteries.[30−32] Extending these salts to aqueous electrolyte for ZIBs would be intriguing, which, however, to the best of our knowledge, has not been reported.

In this study, we report cation-defective $ZnMn_2O_4$ spinel as a new reversible cathode material of aqueous ZIBs. We also comparatively investigate the electrochemical properties of different zinc salts in aqueous solutions. In a rationalized 3 M $Zn(CF_3SO_3)_2$ electrolyte, we show a ∼100% Coulombic efficiency of Zn stripping/plating and fast, highly reversible Zn^{2+} intercalation in the spinel/carbon composite. The new cathode exhibits high specific capacity (∼150 mAh g^{-1} at a current density of 50 mA g^{-1}), long-term cyclability and superior rate capability (94% capacity retention after 500 cycles at 500 mA g^{-1}) within the potential window of 0.8−1.9 V. Furthermore, the kinetics and mechanism of Zn insertion in nonstoichiometric ZMO spinel has been first elucidated by a combination study of electrochemical measurements, X-ray diffraction analysis, Raman/FTIR/NMR spectroscopy, and synchrotron soft X-ray absorption spectroscopy.

EXPERIMENTAL SECTION

Materials and Synthesis. Cation-defective $ZnMn_2O_4$ spinel uniformly composited with conducting carbon (denoted as ZMO/C) was prepared through our recently developed method[33] involving two steps of $NH_3{\cdot}H_2O$-assisted oxidation precipitation and spinel crystallization, as schematically illustrated in Figure S1. In a typical synthesis, 5 mL 0.2 M $Zn(NO_3)_2$, 10 mL 0.2 M $Mn(NO_3)_2$ and 160 mg carbon (Vulcan XC-72) were loaded in a 50 mL flask. Then, 9 mL aqueous ammonia (25 wt %) was dripped into the mixture under constant stirring for 1 h. Afterward, the mixture was evaporated and heated at 180 °C for 3 h, generating ZMO/C composite with 60 wt % spinel and 40 wt % carbon. The product precipitate was centrifuged, washed thoroughly with water and absolute ethanol, and vacuum-dried at 80 °C for 10 h. This mild synthesis can be easily scaled up (Figure S2). For comparsion, neat $ZnMn_2O_4$ (ZMO) without carbon was prepared via conventional ceramic method by calcing the stoichiometric amount of nitrate precursors at 600 °C for 10 h (details described in Supporting Information).

Characterization. Powder X-ray diffraction (XRD) tests were performed on Rigaku MiniFlex600 with Cu Ka radiation. The XRD data was refined by the RIETAN-2,000 Rietveld refinement program.[34] Transmission electron microscopy (TEM) and scanning electron microscopy (SEM) were taken on JEOL 2100F and JEOL JSM-7500F microscopes equipped with energy dispersive spectroscopy (EDS) for elemental analysis. Inductively coupled plasma atomic emission spectroscopy (ICP-AES) was conducted on PerkinElmer Optima 8300. X-ray photoelectron spectroscopy (XPS) was recorded on PerkinElmer PHI 1600 ESCA. Raman spectra were obtained on confocal Thermo-Fisher Scientific DXR microscope using 532 nm excitation. Thermogravimetric (TG) analysis was measured by a Netzsch STA 449 F3 Jupiter analyzer. Fourier transform infrared (FTIR) spectra were collected on Bruker Tensor II. The synchrotron soft X-ray absorption spectroscopy was measured at Beamline20A of Taiwan Synchrotron Radiation Research Center. Solid-state Nuclear Magnetic Resonance (NMR) experiments were performed on a Varian Infinitplus-400 wide-bore (89 mm) NMR spectrometer at a frequency of 399.72 for proton at room temperature under magic angle spinning at 27 kHz.

Electrochemical Tests. Aqueous $ZnCl_2$, $Zn(NO_3)_2$, $ZnSO_4$, and $Zn(CF_3SO_3)_2$ solutions (concentration 1−4 M, as stated) were used as the electrolytes. The saturation concentration is around 3 and 4 M for $ZnSO_4$ and $Zn(CF_3SO_3)_2$, respectively. The Zn plating/stripping properties in different electrolytes were characterized by cyclic voltammograms (CVs) at a potential sweeping rate of 0.5 mV s^{-1}, using a Ti foil as the working electrode and Zn foil as both the reference and counter electrodes. The electrochemical stability and reversibility of electrolytes were tested in symmetrical Zn/Zn cells with two Zn foils and separately 1 M KOH, 3 M $ZnSO_4$ and 3 M $Zn(CF_3SO_3)_2$.

Electrochemical tests of spinel cathode were performed with CR2032 coin-type cells. The cathode was fabricated by mixing the ZMO/C composite and polyvinylidene fluoride (PVDF) with a weight ratio of 9:1 using *N*-methyl-2-pyrrolidone (NMP) as solvent. The same composition (active mass: Vulcan XC-72 carbon: PVDF) was applied to prepare the comparative electrode of ZMO+C (a mechanical mixture of carbon and neat ZMO). The electrode slurry was pasted onto a titanium foil at a loading mass of 2.0 mg cm^{-2} and vacuum-dried at 100 °C for 12 h. Zinc foil and filter paper were employed as the anode and separator, respectively. A 3 M $Zn(CF_3SO_3)_2$ aqueous solution was used as the electrolye. For comparison, the electrode performance was also tested in nonaqueous electrolyte (0.1 M $Zn(CF_3SO_3)_2$ in acetonitrile). Voltametry was conducted on Parstat 263A (AMETEK) between 0.8−2.0 V at a scan rate of 0.2 mV s^{-1}. Galvanostatic charge/discharge data were recorded on a LAND-CT2001A battery-testing instrument. The current density and specific capacity were based on the mass of ZMO in each electrode. Electrochemical impedance spectroscopy (EIS) test was performed on a Parstat 2273 electrochemical workstation (AMETEK) with an AC voltage of 5 mV amplitude in the frequency ranging from 100 kHz to 100 mHz.

RESULTS AND DISCUSSION

Materials Characterization. Figure 1a and Figure S3 show the XRD patterns of the obtained ZMO/C and ZMO samples along with the corresponding Rietveld refinement. All peaks are readily assigned to the space group *I*41/*amd* (no. 141), consistent with the standard values of the body-centered tetragonal $ZnMn_2O_4$ (JCPDS no.77−470). The refined profiles fit well with the experimental data (Table S1, S2) and indicate the formation of spinel structure, in which Zn ions occupy 1/8 of the tetrahedral sites (4a) and Mn ions reside 1/2 of the

DOI: 10.1021/jacs.6b05958
J. Am. Chem. Soc. 2016, 138, 12894−12901

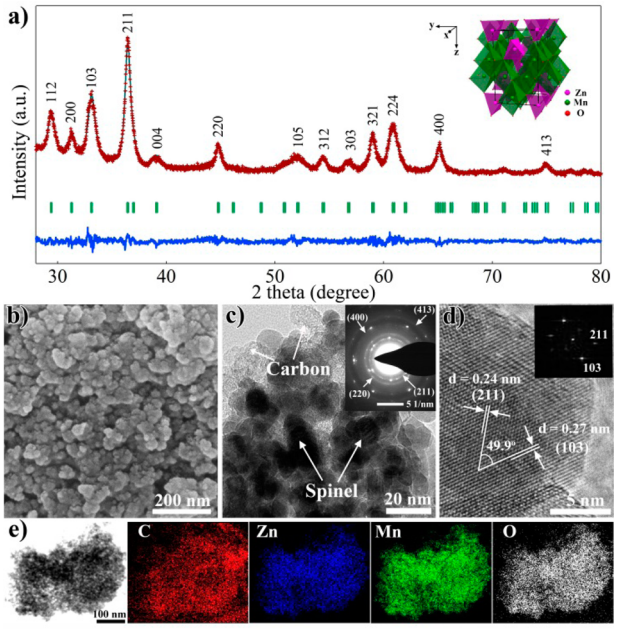

Figure 1. (a) Rietveld refined XRD pattern of ZMO/C. Experimental data, calculated results, allowed Bragg diffraction positions and difference profile are marked with red dots, cyan line, vertical bars and blue curve, respectively. Inset schematically represents the spinel structure. (b) SEM image. (c) TEM and (d) HRTEM images, insets showing the corresponding SAED and FFT patterns, respectively. (e) STEM micrograph with elemental mapping images.

octahedral sites (8d), remaining unoccupied octahedral sites (8c). As carbon in the composite is in amorphous state, we measured the Raman spectra (Figure S4). The strong peak around 670 cm^{-1} is characteristic vibration involving motion of oxygen inside the octahedral MnO_6 unit, while two overlapped peaks centered at around 350 cm^{-1} are ascribed to the Zn−O bond stretching.[35,36] Besides, the peaks at 1330 and 1600 cm^{-1} are indexable to the D band and G band of carbon, respectively.[37] As expected, no carbon Raman signal is discernible for neat ZMO.

Figure 1b shows the typical SEM image of ZMO/C, presenting a nanoparticulate morphology. TEM imaging (Figure 1c) further reveals that the spinel nanograins are uniformly and firmly composited with carbon nanoparticles. The average particle size of spinel ZMO is about 15 nm (Figure S5). Polycrystalline character of ZMO nanoparticles is verified by the selected-area electron diffraction (SAED) pattern. Structural symmetry and crystallinity can be also viewed from the clear lattice fringes in high-resolution TEM (HRTEM) image and the fast Fourier transform (FFT) diffraction pattern (Figure 1d). The neighboring interlayer distances of 0.27 and 0.24 nm correspond respectively to the (103) and (211) planes with interplanar angle of 49.9°, conforming to the allowed Bragg diffraction of tetragonal spinel. Moreover, Figure 1e shows the STEM and the elemental mapping of ZMO/C, evidencing homogeneous distribution of Zn, Mn, O and C components. The neat ZMO synthesized at 600 °C is composed of nanoparticles with average size of 50 nm (Figure S6). The carbon content (40 wt %) in as-prepared ZMO/C was confirmed by TG analysis (Figure S7).

From chemical titration, the mean Mn valence is 3.22 and 3.03 for ZMO/C and neat ZMO, respectively (Supporting Information). EDS and ICP-AES were then performed to determine the compositional ratio of Mn and Zn for the spinel (Figure S8 and Table S3). On the basis of the invariable valence of Zn and O, the higher oxidation state than nominal 3 and the lower Mn:Zn ratio than stoichimetric 2 confirm the presence of Mn vacancies in the spinel. XPS was also carried out to investigate the surface oxidation state of Mn (Figure S9). The fitting of two deconvoluted peaks in Mn 2p spectra suggests the presence of multiple Mn valence. The positive shift of peak position indicates increase of Mn valence from ZMO to ZMO/C, consistent with the titration analysis. Combining the analytical results, the composition of spinels in ZMO/C and neat ZMO can be expressed as $ZnMn_{1.86}Y_{0.14}O_4$ and $ZnMn_{1.98}Y_{0.02}O_4$ (Y denotes vacancy), respectively. Thus, the ZMO/C nanocomposite features abundant cation vacancies and small particle size, which could be attributed to the mild solution-based synthesis (a low temperature of 180 °C and a short time of 3 h) that favors the formation of ultrafine and nonstoichiometric spinels.[27,33,34,38]

Electrolyte Fomulation. The electrochemical stability and Zn stripping/plating efficiency are important factors in the selection of electrolyte for aqueous ZIBs. Alkaline electrolyte such as KOH solution is inappropriate since it results in large polarization for Zn deposition/dissolution reactions and limited cyclability (Figure S10). We also ruled out strong acidic electrolytes considering the vigorous H_2 evolution in them. Thus, four mild acidic solutions separately containing zinc salt of $ZnCl_2$, $ZnNO_3$, $ZnSO_4$ and $Zn(CF_3SO_3)_2$ were investigated.

The potentiodynamic behaviors of Zn electrode are compared in different electrolytes. As shown in Figure 2, the voltammetry in $Zn(CF_3SO_3)_2$ and $ZnSO_4$ solutions indicates reversible electrochemical deposition/dissolution of Zn. Apparently different process is observed in $ZnCl_2$ and $ZnNO_3$ solutions, which is associated with the instability of Cl^- and NO_3^- (Figure S11). Notably, $Zn(CF_3SO_3)_2$ and $ZnSO_4$ solutions exhibit a wide electrochemical window. The parasitical reactions of O_2 evolution are significantly suppressed up to 2.4 and 2.3 V for 1 M $Zn(CF_3SO_3)_2$ and 1 M $ZnSO_4$, respectively (Figure S12). The corresponding onset potentials of initial Zn plating/stripping are −0.14/−0.050 V and −0.17/−0.055 V. Compared to $ZnSO_4$, smaller potential separation between plating and stripping and higher response current can be found for $Zn(CF_3SO_3)_2$, suggesting better reversibility and faster kinetics of Zn deposition/dissolution. The Coulombic efficiency (CE) in $Zn(CF_3SO_3)_2$ electrolyte gradually increased and reached 100% after the third cycle. In comparison, the CE in $ZnSO_4$ electrolyte was lower at each cycle and decreased with cycling (Table S4). The superior electrochemical properties of $Zn(CF_3SO_3)_2$ could be attributed to the bulky $CF_3SO_3^-$ anions (versus SO_4^{2-} with double charge) that decrease the number of water molecules surrounding Zn^{2+} cations and reduce solvation effect, facilitating Zn^{2+} transportation and charge transfer.

For further electrolyte optimization, we prepared $Zn(CF_3SO_3)_2$ solutions with varied salt concentrations. Salt concentration exerts profound effect on physicochemical properties of electrolyte in lithium battery chemistries.[22,39,40] As the $Zn(CF_3SO_3)_2$ concentration increases from 1 to 4 M, the current in voltammograms decreases (Figure 3a), similar to the observation in $Ca(BF_4)_2$ electrolyte for Ca cell and $LiN(SO_2CF_3)_2$ electrolyte for Li cell.[7,39] Meanwhile, the ionic conductivity of the electrolyte decreases whereas the solution viscosity increases (Figure 3b). Previous studies on Li cells have demonstrated that increased viscosity in high-concentration

DOI: 10.1021/jacs.6b05958
J. Am. Chem. Soc. 2016, 138, 12894−12901

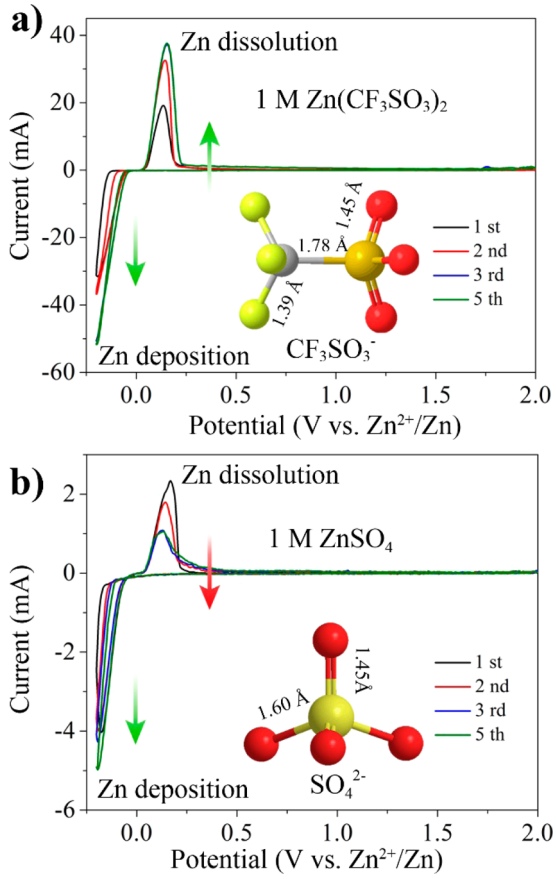

Figure 2. Cyclic voltammograms of Zn electrode in aqueous electrolyte of (a) 1 M $Zn(CF_3SO_3)_2$ and (b) 1 M $ZnSO_4$ at the scan rate of 0.5 mV s^{-1} between −0.2 and 2.0 V.

electrolyte alters the solvation and transporting behaviors of cations/anions to enhance stability and kinetics.[22,39,40] Moreover, higher salt concentration could reduce the water activity and water-induced side reactions, leading to improved cycle stability of electrode in aqueous solutions.[22,41] We envision similar positive attribute of high-concentration $Zn(CF_3SO_3)_2$. For 3 M $Zn(CF_3SO_3)_2$ (pH ∼ 3.6), the O_2 evolution potential was suppressed up to 2.5 V (Figure S13). Importantly, there are no detectable side reactions in 0.8−1.9 V, which is the working voltage window for aqueous ZIBs. In addition, the H_2 evolution potential shifted below −0.3 V (vs Zn^{2+}/Zn) due to the large overpotential on Ti substrate (Figure S14).

The CE of ZMO/C cathode upon cycling in $Zn(CF_3SO_3)_2$ electrolyte increases with salt concentration and reaches almost unchanged at 3 M (Figure 3c). The typical charge/discharge profiles of ZMO/C electrode in 1 M $Zn(CF_3SO_3)_2$ solution are shown in Figure S15. A comparison of the cycling performance in diluted electrolyte and concentrated electrolyte (e.g., 3 M, shown later in Figure 5) clearly indicates superiority of the latter. These observations can be ascribed to alleviated dissolution of active species (i.e., Mn in ZMO spinel) at concentrated electrolyte, as evidenced by analyzing the separator deposit and electrolyte after cycling the cathode (Figures S16,17 and Table S5). Negligible amount of dissolved Mn can be detected with $Zn(CF_3SO_3)_2$ concentration higher than 3 M.

The properties of 3 M $Zn(CF_3SO_3)_2$ electrolyte were further evaluated in Zn/Zn symmetric cells. Symmetric cell configuration is commonly employed in battery chemistries (e.g., Zn-

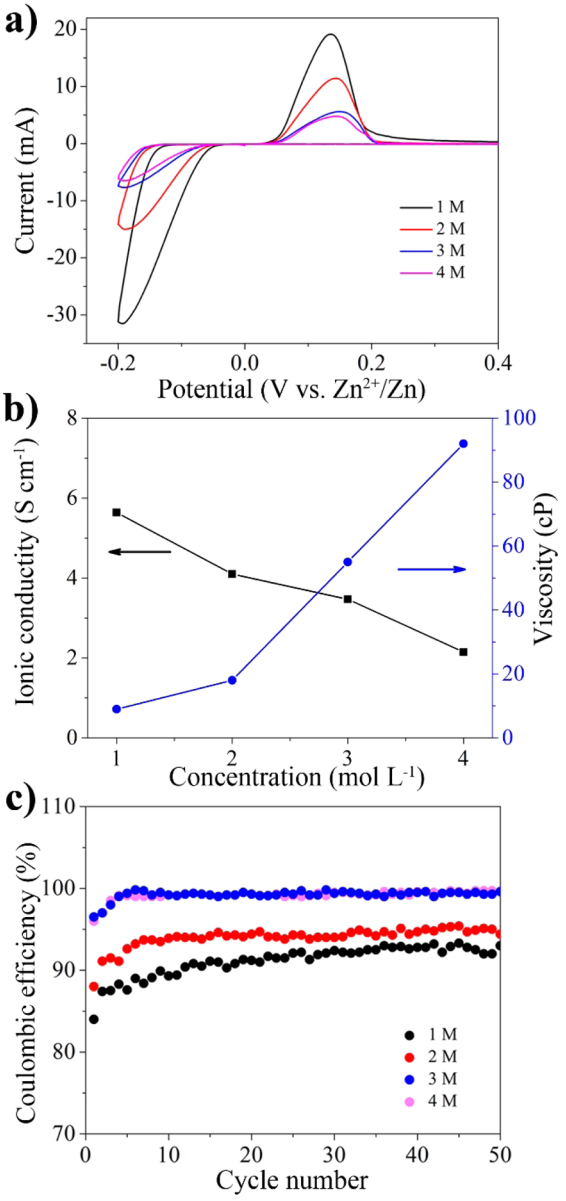

Figure 3. Characterization of aqueous $Zn(CF_3SO_3)_2$ electrolyte with different concentrations (1−4 M): (a) CVs of zinc electrode at potential scanning rate of 0.5 mV s^{-1}, (b) viscosity and ionic conductivity, and (c) CE of ZMO/C electrode as a function of cycle number at current rate of 50 mA g^{-1} within 0.8−1.9 V.

based[16,19,31,42,43] and Li-based[44,45] systems) for fundamental studies on the intrinsic properties of electrolytes due to merits such as permitting high rates of charge/discharge, circumventing the need of a complementary electrode, and eliminating the effect of undesired reactions associated with counter electrode. Figure 4a displays the typical voltage profiles at a constant charge and discharge current density of 0.1 mA cm^{-2}. Good reversibility of Zn stripping/plating can be observed for both the $Zn(CF_3SO_3)_2$ electrolyte and the comparative $ZnSO_4$ electrolyte that has been extensively employed in rechargeable Zn-MnO_2 batteries.[11,14−16] As viewed from the enlarged curves at different cycles (Figure 4a inset), the $Zn(CF_3SO_3)_2$ electrolyte shows a decrease of overpotential upon cycling, whereas $ZnSO_4$ exhibits apparently large overpotential and augment of charge−discharge voltage separation, indicating higher energy efficiency in $Zn(CF_3SO_3)_2$. Interestingly, the

DOI: 10.1021/jacs.6b05958
J. Am. Chem. Soc. 2016, 138, 12894−12901

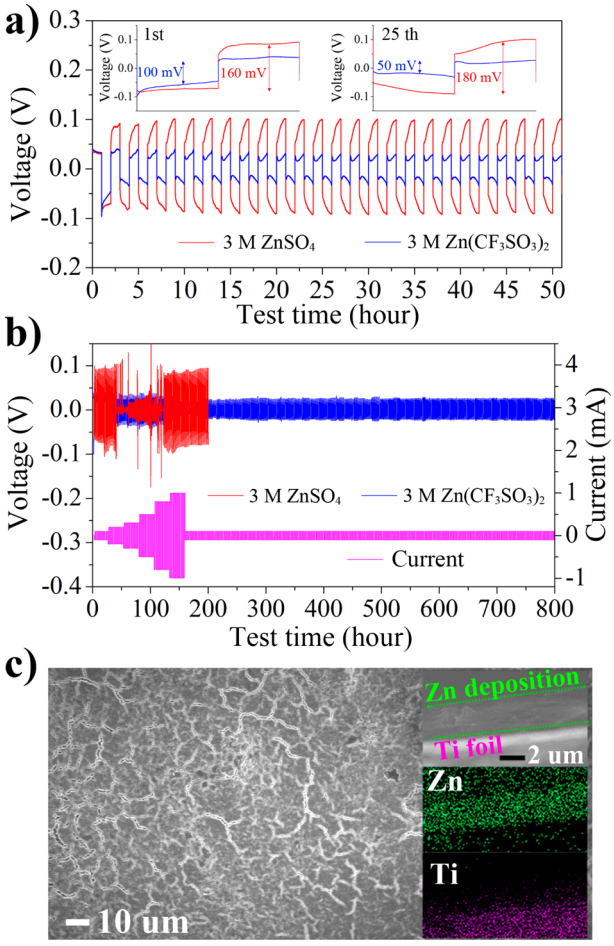

Figure 4. (a) Galvanostatic cycling of Zn/Zn symmetrical cells at 0.1 mA cm^{-2} in 3 M $ZnSO_4$ and 3 M $Zn(CF_3SO_3)_2$ electrolytes. Insets enlarge the voltage profiles of the first and 25th cycles. (b) Rate performance and long-term cyclability of Zn/Zn symmetrical cells in 3 M $ZnSO_4$ and 3 M $Zn(CF_3SO_3)_2$ electrolytes. (c) SEM images and elemental mapping of Zn deposit on Ti foil obtained at −0.2 V vs Zn^{2+}/Zn during the 0.5 mV s^{-1} CV test in 3 M $Zn(CF_3SO_3)_2$.

potential profiles remain almost unchanged as the test current increases from 0.1 to 1.0 mA cm^{-2} (Figure 4b), showing excellent rate capability. More importantly, the reversibility can be sustained for 800 h, indicating extremely high stability. Tests in unsymmetrical Zn/Ti cells also confirms the significantly better durability of $Zn(CF_3SO_3)_2$ over the $ZnSO_4$ counterpart (Figure S18). At the typical deposition potential of −0.2 V, a uniform layer of Zn grows on Ti foil, without the formation of detrimental dendrite (Figure 4c) and byproducts such as ZnO or $Zn(OH)_2$ (Figure S19). Taking into consideration a compromise among loading and performance, we selected 3 M $Zn(CF_3SO_3)_2$ solution as the electrolyte, which characterizes a wide stable potential window up to 2.5 V, an ionic conductivity of 3.47 S cm^{-1}, and a ∼100% CE for both Zn anode and ZMO/C cathode.

Electrode Performance. The electrode properties of the cation-defective spinel cathode were investigated using coin cells employing Zn foil anode, 3 M $Zn(CF_3SO_3)_2$ electrolyte, and filter paper separator. Figure 5a displays the CV curves of ZMO/C scanned at 0.2 mV s^{-1}. The profile in the initial cycle slightly differs from the followed ones, which can be related to the gradual activation of the electrode, similar to the observation from MnO_2-based cathodes in ZIBs.[14,15] Upon cycling, the electrode polarization decreases, as indicated by EIS analysis (Figure S20). On anodic sweeping, two peaks centered at around 1.55 and 1.6 V appear and overlap, tentatively corresponding to stepwise electrochemical Zn^{2+} extraction from the spinel. In cathodic scans, two distinct peaks are observed at around 1.35 and 1.1 V, which are feasibly attributed to gradual intercalation of Zn^{2+} into the spinel framework. For spinel $LiMn_2O_4$, two couples of reversible redox peaks can be observed as well, corresponding to the two-step extraction/insertion as Li^+ goes through a Li-rich state and a Li-depleted state.[10,22−24] Similarly, it is reasonable to postulate that Zn ions extract/insert step by step from the tetrahedral sites of spinel ZMO framework, undergoing a Zn-rich state and a Zn-depleted state. Furthermore, the CVs remain invariable after the third cycle, demonstrating good reversibility of the electrode.

Figure 5b shows the charge/discharge curves of the ZMO/C electrode cycled at the current rate of 50 mA g^{-1} within 0.8−1.9 V. The ZMO/C composite delivers initial specific charge and discharge capacities of 128 and 120 mAh g^{-1}, respectively. After three cycles, the electrode maintains stable capacities at around 150 mAh g^{-1} with high CE around 100%. The average

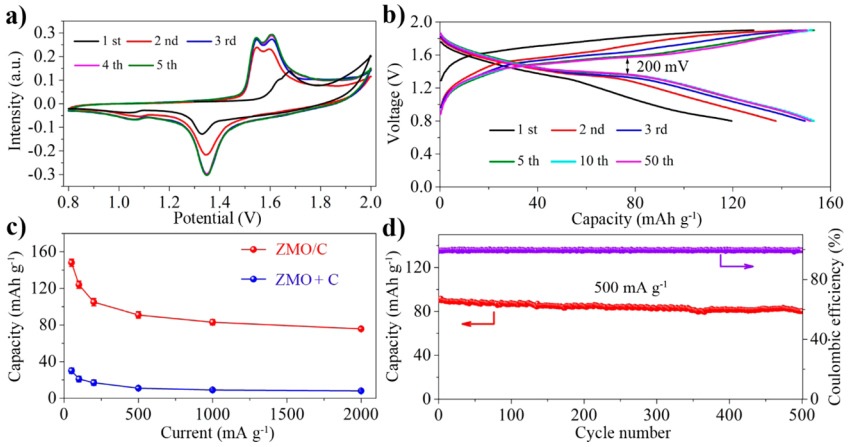

Figure 5. (a) CVs of ZMO/C electrode scanning at 0.2 mV s^{-1} in 3 M $Zn(CF_3SO_3)_2$ electrolyte using Zn-ZMO/C coin cells. (b) Galvanostatic charge/discharge curves of ZMO/C between 0.8 and 1.9 V at 50 mA g^{-1}. (c) Rate performance of ZMO/C composite and ZMO+C mixture. (d) Cycling performance of ZMO/C at 500 mA g^{-1}.

DOI: 10.1021/jacs.6b05958
J. Am. Chem. Soc. 2016, 138, 12894−12901

discharge voltage plateau is 1.35 V, giving an energy density of ~202 Wh kg^{-1} based on the active mass. Roughly assuming that the cathode material occupies 1/3 of the total weight in a pouch cell configuration,[46] the ZMO/C nanocomposites afford an estimated energy density of 70 Wh kg^{-1}, which is much higher than that of other aqueous Li-ion batteries[22,47] as well as commercial Pb-acid (~30 Wh kg^{-1}) and Ni−Cd (~50 Wh kg^{-1}) battery technologies.[48] In comparison, the ZMO+C mixture (40 wt % carbon) gives a significantly lower capacity of 37 mAh g^{-1} at 50 mA g^{-1} (Figure 5c). Note that the carbon matrix contributes to a negligible capacity (<2 mAh g^{-1}) even at a low current density of 10 mA g^{-1} (Figure S21). Furthermore, neat ZMO prepared at 600 °C exhibits poor electrode performance (reversible capacity ~42 mAh g^{-1}) although its average particle size is significantly decreased from 50 to 23 nm (Figure S22). These results suggest that the cation-deficient ZMO is the main attribution to the remarkable capacity of ZMO/C composite while limited amount of Zn^{2+} can be extracted from ZMO synthesized from traditional firing process.

Besides higher capacity, the ZMO/C composite manifests superior rate performance to ZMO+C mixture, as shown in Figure 5c. A considerable capacity of 72 mAh g^{-1} is attained at a high current rate of 2000 mA g^{-1}. For the evaluation of long-term cycling stability, the ZMO/C electrode is further galvanostatically charged and discharged at 500 mA g^{-1}. Remarkably, a capacity retention of 94% is obtained up to 500 cycles, showing excellent cyclability among reported aqueous ZIBs (Table S6).[11,13−18] After cycling, the morphology of ZMO/C is essentially preserved with ZMO nanograins uniformly composited with the conducting carbon particles and, the spinel structure is well maintained as well (Figure S23). In addition, post-mortem examination of cycled Zn anode reveals that the anode shows a dendrite-free and dense surface morphology after 50 repeated cycles, without the formation of byproducts such as ZnO or $Zn(OH)_2$ (Figure S24).

Electrochemical Mechanism Studies. We coupled electrochemical investigations and structural analysis to understand the electrode behaviors and reaction mechanism of ZMO. Figure 6a shows the typical galvanostatic charge/discharge curves of ZMO/C at the stabilized third cycle, where the average potential positions of the two-stage slopping plateaus agree with the voltammogram observation (Figure 4a). To elucidate the evolution of ZMO spinel during Zn insertion/extraction, ex situ XRD, Raman spectra and synchrotron soft X-ray absorption spectroscopies (sXAS) were conducted at selected charge/discharge states (marked points in Figure 6a). In survey XRD profiles (Figure S25), there are no extra signals besides peaks of ZMO, evidencing that the spinel structure is maintained during the extraction/insertion process. As shown in the enlarged patterns within 2θ range of 30−38° (Figure 6b), the characteristic diffraction peaks gradually shift to higher angle on charging from 0.8 to 1.9 V, which indicates the shrinking of crystal lattice due to the extraction of tetrahedral site cations (i.e., Zn^{2+}) from the spinel. The spinel ZMO structure is recovered upon full discharging back to 0.8 V.

Raman spectra and the corresponding Lorentzian fitting (Figure 6c and Table S7) provide further structural information on the spinel electrode at different charge/discharge states. A pair of overlapped low-intensity peaks (325/375 cm^{-1}) and a strong absorption at around 670 cm^{-1} are ascribed to Zn−O and Mn−O vibrations in ZMO spinel, respectively.[35,36,49] On charging, the peak associated with Zn−O bond stretching is

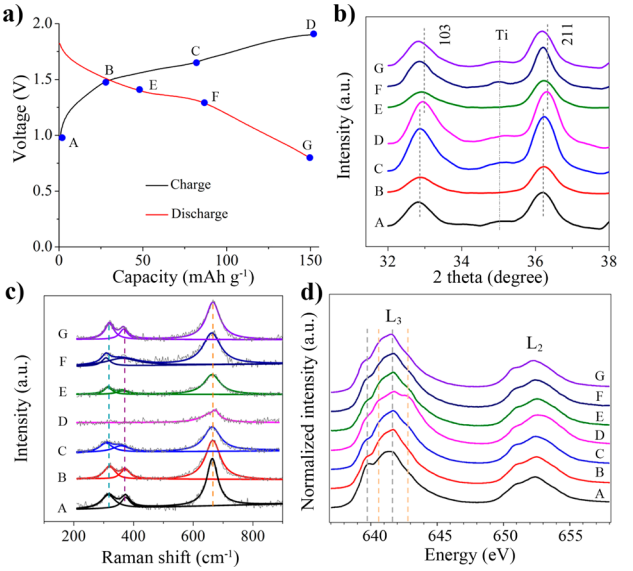

Figure 6. (a) Charge/discharge curves (third cycle) of ZMO/C electrode at 50 mA g^{-1} in 3 M $Zn(CF_3SO_3)_2$ electrolyte. The points marked the states where data were collected for analysis. (b) XRD patterns within selected angle (2θ) of 30−38°. (c) Raman spectra (gray curves) and Lorentzian fitting (colored solid profiles) in the wavenumber range of 200−900 cm^{-1}. (d) sXAS of Mn *L*-edge spectra.

weakened due to the extraction of Zn^{2+} cations. As expected, reverse discharging increases the peak intensity. The progressive variation of recovery of the singlet peak, owing to the shrinking and expanding of crystal lattice caused by Zn^{2+} removal/insertion, is in line with the XRD analysis.

sXAS is an incisive technique to analyze the oxidation state and electronic properties of electrode materials.[50,51] Mn *L*-edge sXAS (Figure 6d) gives a direct probe of 3*d* unoccupied states of Mn through dipole-allowed 2*p*-to-3*d* transitions. The multiplet features due to crystal field splitting in the L_3 region, i.e., peaks located at 640.5 and 642.9 eV are considered as the fingerprint of Mn^{4+}, while the peaks at 639.7 and 641.7 eV correspond to Mn^{3+} oxidation state.[28,52] The gradual emerging and vanishing of these peaks unambiguously witness the electron transfer involved in the Mn^{3+}/Mn^{4+} redox couple during the charge/discharge processes. The presence of tetravalent Mn coincides well with the value calculated from the specific charge capacity of cation-defected ZMO having a determined composition of $ZnMn_{1.86}Y_{0.14}O_4$.

Previous studies have demonstrated that proton insertion is not involved in the spinel $LiMn_2O_4$ cathode in aqueous acidic media.[10,53−55] To figure out the issue whether proton inserts into the spinel $ZnMn_2O_4$ lattice in $Zn(CF_3SO_3)_2$ electrolyte, we further carried out a series of analytical studies, including FTIR, ^1H solid state NMR, TEM-EDS, ICP and electrochemical investigations. Supposing H^+ ions insert into the spinel structure, they would bind to oxygen, forming species with O−H group (e.g., MnOOH).[53] However, besides absorbed H_2O, vibrations of O−H bonding in charged or discharged ZMO could not be detected in FTIR spectra (Figure S26) or NMR spectra (Figure S27). In addition, elemental analysis from TEM-EDS (Figure S28) and ICP analysis (Table S8) show that the Zn content significantly decreased at fully charged state, and was recovered on fully discharging. Moreover, the ZMO/C electrode could deliver a reversible capacity of ~90 mAh g^{-1} in nonaqueous electrolyte (0.1 M $Zn(CF_3SO_3)_2$ in acetonitrile

DOI: 10.1021/jacs.6b05958
J. Am. Chem. Soc. 2016, 138, 12894−12901

solution) (Figure S29), while it could be hardly charged/discharged in a buffer solution (potassium hydrogen phthalate with pH = 4) without Zn^{2+} ions (Figure S30). A combination of these results and the data shown in Figure 6 clearly confirms that the electrochemical behaviors of ZMO spinel arise from reversible insertion of Zn^{2+} ions rather than proton intercalation.

According to the above analysis, we propose that the electrochemical reaction occurs in ZMO spinel electrode follows $ZnMn_{1.86}Y_{0.14}O_4 \leftrightarrow Zn_{1-x}Mn_{1.86}Y_{0.14}O_4 + 2xe^- + xZn^{2+}$ ($0 < x < 1$), where x denotes the number of reversibly extracted Zn^{2+} and is up to 0.7 in this study. On charge or discharge, Zn^{2+} extracts from or inserts into the Zn−O tetrahedron sites of ZMO spinel (Figure 7a). The basic spinel

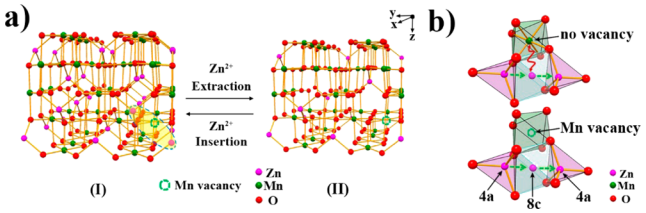

Figure 7. (a) Schematic illustration of Zn^{2+} insertion/extraction in an extended three-dimensional ZMO spinel framework. (b) Proposed Zn^{2+} diffusion pathway in ZMO spinel without and with Mn vacancies.

lattice is maintained during the charge and discharge process, resembling the case of spinel $LiMn_2O_4$ in aqueous LIB.[21] We suggest that the presence of abundant Mn vacancies in $ZnMn_{1.86}Y_{0.14}O_4$ is a peculiar merit for Zn^{2+} diffusion in the spinel framework, as schematically shown in Figure 7b. In perfect spinel without cation deficiency, Zn^{2+} ions migrate from one tetrahedral site (4a) to another by passing through an unoccupied octahedral site (8c) and thus bear a large electrostatic repulsion from Mn cations in a neighboring octahedral site (8d), strongly impeding Zn^{2+} diffusion. Difficult Zn diffusion in ideal spinel has been demonstrated by previous studies on chemical extraction of Zn from spinel oxide synthesized at high temperature.[25] In comparison, the spinel rich in Mn vacancies allows for easier Zn-ion diffusion without much electrostatic barrier, leading to higher mobility of Zn^{2+} cations and consequently faster electrode kinetics.

The diffusion coefficient of Zn^{2+} (D_{Zn}) in Mn-defected ZMO spinels was determined by the galvanostatic intermittent titration technique (GITT) (details described in Supporting Information). As shown in Figure 8, the average D_{Zn} values at the charge and discharge plateaus are about 0.4×10^{-11} and 1.0×10^{-11} cm^2 s^{-1}, respectively. This Zn diffusivity is comparable with Li diffusion coefficient (normally at magnitude of $\sim 10^{-10}$ cm^2 s^{-1}) in spinel cathode.[1,48] In contrast, the ZMO+C electrode exhibits a lower D_{Zn} (1.1×10^{-13} cm^2 s^{-1} at charge platform) and a larger overpotential, as it features significantly less cation deficiency, resulting in sluggish mobility during charge/discharge process. Besides beneficial ionic diffusion, the cation-vacant ZMO spinel also favors charge transfer, as viewed from the EIS analysis (Figure S31a). The charge-transfer resistance of ZMO/C is 280 Ω, which is much lower than that of ZMO+C (1000 Ω). Furthermore, ZMO/C possesses an electrical conductivity of 2.0 S m^{-1} (Figure S31b), exceeding triple that of ZMO+C.

For manganese oxides, nanostructuring and the presence of defects play important roles in enhancing the transporting

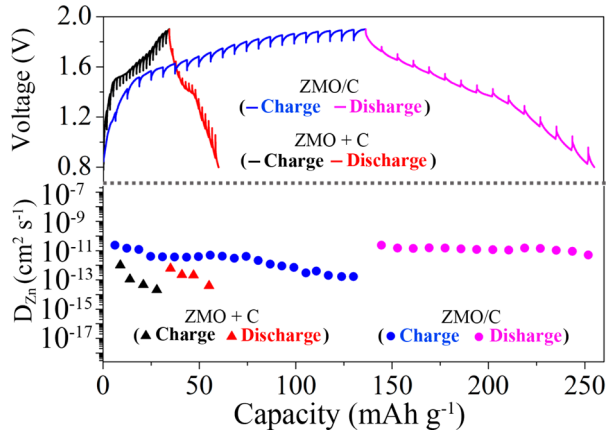

Figure 8. GITT profiles and calculated Zn^{2+} diffusion coefficient of ZMO/C and ZMO+C electrodes.

properties and electrochemical performance.[56,57] Nanosized electrode materials intrinsically benefit rapid ionic diffusion due to short transport distance and could better accommodate the structural strain through slippage at domain boundaries, thus enhancing the cyclability of spinel.[58,59] The ZMO/C electrode bearing small spinel nanoparticles, abundant Mn vacancies and strong oxide-carbon coupling allows facile electron conduction, charge transfer and ionic diffusion, resulting in high reversible capacity and respectable rate capability that cannot be gained in ZMO synthesized from conventional ceramic route. Compared to the stoichiometric $ZnMn_2O_4$ spinel, the higher average oxidation state (i.e., 3.22) of Mn in cation-deficient ZMO is another advantageous factor to alleviate Jahn−Teller structural distortion and disproportionation caused by Mn(III). Furthermore, the use of high-concentration $Zn(CF_3SO_3)_2$ electrolyte helps to mitigate the dissolution of electrochemically active Mn species since the bulky anions and high slat concentration could reduce the water activity and water-induced side reactions. We expect that other zinc salts containing large anions such as $Zn(TFSI)_2$ is applicable as well.

CONCLUSION

In conclusion, we have demonstrated the application of cation-defected $ZnMn_2O_4$ spinel as a new stable cathode material for rechargeable aqueous Zn-ion batteries. In a formulated novel electrolyte of 3 M aqueous $Zn(CF_3SO_3)_2$, the obtained ZMO/C hybrid bearing abundant cation vacancies exhibits a reversible specific capacity of 150 mAh g^{-1} at 50 mA g^{-1} and an unprecedented capacity retention of 94% after 500 cycles at high rate of 500 mA g^{-1}. The remarkable electrode performance can be attributed to the cation-defected ZMO spinel that permits fast, repeated Zn insertion/extraction and the Zn-$(CF_3SO_3)_2$ electrolyte that not only enables wide electrochemical window (2.5 V), high Zn plating/stripping efficiency and long-term stability but effectively mitigates the loss of Mn species from ZMO spinel. These results suggest the importance of cation nonstoichiometry in the search of advanced electrode materials for insertion of multivalent metal-ion. This study also indicates that the shift from binary transition metal oxide to composite spinel oxides and the use of an electrolyte salt comprising bulky anion (e.g., $CF_3SO_3^-$) may open a new avenue to develop rechargeable aqueous zinc batteries with high safety, low cost and environmental benignity.

DOI: 10.1021/jacs.6b05958
J. Am. Chem. Soc. 2016, 138, 12894−12901

■ ASSOCIATED CONTENT

Supporting Information

The Supporting Information is available free of charge on the ACS Publications website at DOI: 10.1021/jacs.6b05958.

Additional experimental details, materials characterization and electrochemical results. (PDF)

■ AUTHOR INFORMATION

Corresponding Author

*fycheng@nankai.edu.cn

Notes

The authors declare no competing financial interest.

■ ACKNOWLEDGMENTS

This work was supported by NSFC (21322101, 21231005, 21473235, and 11227902) and MOE (B12015, ACET-13-0296 and IRT13R30).

■ REFERENCES

(1) Whittingham, M. S. *Chem. Rev.* **2004**, *104*, 4271.
(2) Armand, M.; Tarascon, J. M. *Nature* **2008**, *451*, 652.
(3) Muldoon, J.; Bucur, C.; Gregory, T. *Chem. Rev.* **2014**, *114*, 11683.
(4) Yabuuchi, N.; Kubota, K.; Dahbi, M.; Komaba, S. *Chem. Rev.* **2014**, *114*, 11636.
(5) Choi, J. W.; Aurbach, D. *Nat. Rev. Mater.* **2016**, *1*, 16013.
(6) Lin, M. C.; Gong, M.; Lu, B.; Wu, Y.; Wang, D. Y.; Guan, M.; Angell, M.; Chen, C.; Yang, J.; Hwang, B. J.; Dai, H. J. *Nature* **2015**, *520*, 324.
(7) Ponrouch, A.; Frontera, C.; Barde, F.; Palacin, M. R. *Nat. Mater.* **2016**, *15*, 169.
(8) Li, S.; Dong, Y.; Xu, L.; Xu, X.; He, L.; Mai, L. *Adv. Mater.* **2014**, *26*, 3545.
(9) Lu, Y.; Goodenough, J. B.; Kim, Y. *J. Am. Chem. Soc.* **2011**, *133*, 5756.
(10) Kim, H.; Hong, J.; Park, K. Y.; Kim, H.; Kim, S. W.; Kang, K. *Chem. Rev.* **2014**, *114*, 11788.
(11) Xu, C.; Li, B.; Du, H.; Kang, F. *Angew. Chem., Int. Ed.* **2012**, *51*, 933.
(12) McLarnon, F. R.; Cairns, E. J. *J. Electrochem. Soc.* **1991**, *138*, 645.
(13) Shen, Y.; Kordesch, K. *J. Power Sources* **2000**, *87*, 162.
(14) Alfaruqi, M. H.; Mathew, V.; Gim, J.; Kim, S.; Song, J.; Baboo, J. P.; Choi, S. H.; Kim, J. *Chem. Mater.* **2015**, *27*, 3609.
(15) Lee, B.; Lee, H. R.; Kim, H.; Chung, K. Y.; Cho, B. W.; Oh, S. H. *Chem. Commun.* **2015**, *51*, 9265.
(16) Pan, H.; Shao, Y.; Yan, P.; Cheng, Y.; Han, K. S.; Nie, Z.; Wang, C.; Yang, J.; Li, X.; Bhattacharya, P.; Mueller, K. T.; Liu, J. *Nat. Energy* **2016**, *1*, 16039.
(17) Zhang, L.; Chen, L.; Zhou, X.; Liu, Z. *Adv. Energy Mater.* **2015**, *5*, 1400930.
(18) Trócoli, R.; La Mantia, F. *ChemSusChem* **2015**, *8*, 481.
(19) Liu, Z.; Pulletikurthi, G.; Endres, F. *ACS Appl. Mater. Interfaces* **2016**, *8*, 12158.
(20) Islam, M. S.; Fisher, C. A. J. *Chem. Soc. Rev.* **2014**, *43*, 185.
(21) Li, W.; Dahn, J. R.; Wainwright, D. S. *Science* **1994**, *264*, 1115.
(22) Suo, L.; Borodin, O.; Gao, T.; Olguin, M.; Ho, J.; Fan, X.; Luo, C.; Wang, C.; Xu, K. *Science* **2015**, *350*, 938.
(23) Qu, Q.; Fu, L.; Zhan, X.; Samuelis, D.; Maier, J.; Li, L.; Tian, S.; Li, Z.; Wu, Y. P. *Energy Environ. Sci.* **2011**, *4*, 3985.
(24) Lu, J.; Zhan, C.; Wu, T.; Wen, J.; Lei, Y.; Kropf, A. J.; Wu, H.; Miller, D. J.; Elam, J. W.; Sun, Y. K.; Qiu, X.; Amine, K. *Nat. Commun.* **2014**, *5*, 5693.
(25) Knight, J. C.; Therese, S.; Manthiram, A. *J. Mater. Chem. A* **2015**, *3*, 21077.
(26) Chen, D.; Chen, C.; Baiyee, Z. M.; Shao, Z.; Ciucci, F. *Chem. Rev.* **2015**, *115*, 9869.
(27) Sanchez, L.; Pereira-Ramos, J. P. *J. Mater. Chem.* **1997**, *7*, 471.
(28) Kim, C.; Phillips, P. J.; Key, B.; Yi, T.; Nordlund, D.; Yu, Y. S.; Bayliss, R. D.; Han, S. D.; He, M.; Zhang, Z.; Burrell, A. K.; Klie, R. F.; Cabana. *Adv. Mater.* **2015**, *27*, 3377.
(29) Han, S. D.; Rajput, N. N.; Qu, X.; Pan, B.; He, M.; Ferrandon, M. S.; Liao, C.; Persson, K. A.; Burrell, A. K. *ACS Appl. Mater. Interfaces* **2016**, *8*, 3021.
(30) Guerfi, A.; Trottier, J.; Boyano, I.; De Meatza, I.; Blazquez, J. A.; Brewer, S.; Ryder, K. S.; Vijh, A.; Zaghib, K. *J. Power Sources* **2014**, *248*, 1099.
(31) Kumar, G. G.; Sampath, S. *Solid State Ionics* **2003**, *160*, 289.
(32) Guisao, J. P. T.; Romero, A. J. F. *Electrochim. Acta* **2015**, *176*, 1447.
(33) Li, C.; Han, X.; Cheng, F.; Hu, Y.; Chen, C.; Chen, J. *Nat. Commun.* **2015**, *6*, 7345.
(34) Cheng, F.; Shen, J.; Peng, B.; Pan, Y.; Tao, Z.; Chen, J. *Nat. Chem.* **2011**, *3*, 79.
(35) Malavasi, L.; Galinetto, P.; Mozzati, M. C.; Azzoni, C. B.; Flor, G. *Phys. Chem. Chem. Phys.* **2002**, *4*, 3876.
(36) Hadžić, B.; Romčević, N.; Romčević, M.; Kuryliszyn-Kudelska, I.; Dobrowolski, W.; Wróbel, R.; Narkiewicz, U.; Sibera, D. *J. Alloys Compd.* **2014**, *585*, 214.
(37) Han, X.; Liu, Y.; Jia, Z.; Chen, Y.; Wan, J.; Weadock, N.; Gaskell, K.; Li, T.; Hu, L. *Nano Lett.* **2014**, *14*, 139.
(38) Sanchez, L.; Farcy, J.; Pereira-Ramos, J. P.; Hernan, L.; Morales, J.; Tirado, J. L. *J. Mater. Chem.* **1996**, *6*, 37.
(39) Suo, L.; Hu, Y. S.; Li, H.; Armand, M.; Chen, L. Q. *Nat. Commun.* **2013**, *4*, 1481.
(40) Yamada, Y.; Furukawa, K.; Sodeyama, K.; Kicuchi, K.; Yaegashi, M.; Tateyama, Y.; Yamada, A. *J. Am. Chem. Soc.* **2014**, *136*, 5039.
(41) Ramanujapuram, A.; Gordon, D.; Magasinski, A.; Ward, B.; Nitta, N.; Huang, C.; Yushin, G. *Energy Environ. Sci.* **2016**, *9*, 1841.
(42) Parker, J. F.; Chervin, C. N.; Nelson, E. S.; Rolison, D. R.; Long, J. W. *Energy Environ. Sci.* **2014**, *7*, 1117.
(43) Simons, T. J.; MacFarlane, D. R.; Forsyth, M.; Howlett, P. C. *ChemElectroChem* **2014**, *1*, 1688.
(44) Burns, J. C.; Krause, L. J.; Le, D. B.; Jensen, L. D.; Smith, A. J.; Xiong, D.; Dahn, J. R. *J. Electrochem. Soc.* **2011**, *158*, A1417.
(45) Lu, Y.; Tu, Z.; Archer, L. A. *Nat. Mater.* **2014**, *13*, 961.
(46) Hanssoun, J.; Lee, K. S.; Sun, Y. K.; Scrosati, B. *J. Am. Chem. Soc.* **2011**, *133*, 3139.
(47) Luo, J. Y.; Cui, W. J.; He, P.; Xia, Y. Y. *Nat. Chem.* **2010**, *2*, 760.
(48) Linden, D.; Reddy, T. *Handbook of Batteries*, 3rd ed.; McGraw-Hill: New York, 2002.
(49) Polverejan, M.; Villegas, J. C.; Suib, S. L. *J. Am. Chem. Soc.* **2004**, *126*, 7774.
(50) Ma, X.; Luo, W.; Yan, M.; He, L.; Mai, L. *Nano Energy* **2016**, *24*, 165.
(51) Liu, X.; Yang, W.; Liu, Z. *Adv. Mater.* **2014**, *26*, 7710.
(52) Cramer, S. P.; DeGroot, F. M. F.; Ma, Y.; Chen, C. T.; Sette, F.; Kipke, C. A.; Eichhorn, D. M.; Chan, M. K.; Armstrong, W. H. *J. Am. Chem. Soc.* **1991**, *113*, 7937.
(53) Venkatraman, S.; Manthiram, A. *J. Solid State Chem.* **2004**, *177*, 4244.
(54) Cachet-Vivier, C.; Bach, S.; Pereira-Ramos, J. P. *Electrochim. Acta* **1999**, *44*, 2705.
(55) Mohan Rao, M.; Jayalakshmi, M.; Schäf, O.; Wulff, H.; Guth, U.; Scholz, F. *J. Solid State Electrochem.* **2001**, *5*, 50.
(56) Cai, Z.; Xu, L.; Yan, M.; Han, C.; He, L.; Hercule, K. M.; Niu, C.; Yuan, Z.; Xu, W.; Qu, L.; Zhao, K.; Mai, L. *Nano Lett.* **2015**, *15*, 738.
(57) Tompsett, D. A.; Parker, S. C.; Islam, M. S. *J. Am. Chem. Soc.* **2014**, *136*, 1418.
(58) Xin, S.; Guo, Y. G.; Wan, L. J. *Acc. Chem. Res.* **2012**, *45*, 1759.
(59) Bruce, P. G.; Scrosati, B.; Tarascon, J. M. *Angew. Chem., Int. Ed.* **2008**, *47*, 2930.

DOI: 10.1021/jacs.6b05958
J. Am. Chem. Soc. 2016, 138, 12894−12901